

Detection and Location of the Oceanic Intraplate Earthquakes at the Oldest Pacific Plate Using Pacific Array (Oldest-1) Data

Jun Yong Park¹, YoungHee Kim^{*1}, Takehi Isse², Sang-Mook Lee¹, Kwang-Hee Kim³, Hitoshi Kawakatsu^{2,4}, Hajime Shiobara², Hisashi Utada², Nozomu Takeuchi², and Hiroko Sugioka⁵

Abstract

Oceanic intraplate earthquakes are closely associated with seafloor geologic features, such as knolls, fracture zones, and seamounts. However, this inference is often challenged by significant earthquake location uncertainties and difficulties in detecting small earthquakes, largely owing to limited station coverage. In this study, we used ocean-bottom seismometer data from the Oldest-1 array consisting of 12 sites, which is part of the Pacific array, to construct a one-year earthquake catalog for intraplate events on the oldest Pacific plate (~170–180 Ma), ~900 km east of the Mariana trench. This catalog includes 17 small intraplate earthquakes of magnitude $m_b(Sn)$ 0.9–3.7 that occur within the array (<700 km from the array center). Although their small magnitudes and sparse station coverage, with an average interstation distance of ~393 km did not permit the estimation of focal depths and mechanisms, (re)located events with horizontal location errors of 2–8 km highlight a clear zone of deformation within the plate. Of the 17 earthquakes, 13 occurred in close proximity to seafloor geologic features. We found that five events with $m_b(Sn)$ 0.9–1.6, located near knolls, exhibited high waveform similarity (correlation coefficient exceeding 0.92) and colocation within an $80 \times 80 \text{ m}^2$ area, suggesting that they could be repeating earthquakes. The occurrence of five other events with $m_b(Sn)$ 1.3–2.2 at/near an old fracture zone (~160 Ma) may indicate that the fracture zone may be seismically active regardless of its age. Conversely, three events with $m_b(Sn)$ 2.9–3.7, which show clear T-phase signals are located near seamounts, suggesting the reactivation of pre-existing faults. Our results provide a tighter spatial correlation between epicenters and zones of existing weakness on the seafloor as well as an avenue for detailing waveform characteristics in future experiments.

Introduction

According to plate tectonics theory, a tectonic plate is an internally stable and rigid plate body for which deformation is mainly focused on its margins (Kreemer *et al.*, 2014). Nevertheless, numerous earthquakes have occurred within plates, indicating that the plate interior is also subject to deformation (Schulte and Mooney, 2005). Thus, intraplate seismic activity is essential for advancing our understanding of plate rheology, structure, and the driving forces of plate motion and planetary evolution (e.g., Wiens and Stein, 1985; Gordon, 1998). Although many detailed investigations of intraplate earthquakes have been conducted on continents, particularly those associated with zones of weakness (e.g., Dentith and Featherstone, 2003; Gangopadhyay and Talwani, 2003; Schulte and Mooney, 2005; Chen *et al.*,

2014), the seismicity of the oceanic plate interior remains less explored.

1. School of Earth and Environmental Sciences, Seoul National University, Seoul, Republic of Korea, <https://orcid.org/0000-0003-2244-0210> (JYP); <https://orcid.org/0000-0002-1111-632X> (YHK); <https://orcid.org/0000-0002-8032-0316> (S-ML); 2. Earthquake Research Institute, The University of Tokyo, Tokyo, Japan, <https://orcid.org/0000-0001-9087-8711> (TI); <https://orcid.org/0000-0001-9161-5024> (HK); <https://orcid.org/0000-0002-3319-6383> (HS); <https://orcid.org/0000-0001-5885-5675> (HU); <https://orcid.org/0000-0003-3636-7800> (NT); 3. Department of Geological Sciences, Pusan National University, Busan, Republic of Korea, <https://orcid.org/0000-0001-9931-7996> (K-HK); 4. Institute of Earth Sciences, Academia Sinica, Taipei, Taiwan; 5. Graduate School of Science, Kobe University, Kobe, Hyogo, Japan, <https://orcid.org/0000-0003-1883-4049> (HS)

*Corresponding author: youngkim@snu.ac.kr

© Seismological Society of America

Intraplate earthquakes have been previously observed in the western part of the Pacific plate, which is the oldest part of the oceanic plate (160–180 Ma) (Walker and McCreery, 1985; Wysession et al., 1991). This observation challenges conventional plate tectonics theory, which predicts that old oceanic plates that are relatively cold, thick, and distant from plate boundaries are seismically stable (Wiens and Stein, 1983; Bergman, 1986). Unfortunately, the accuracy of their earthquake locations is inevitably low because of several critical factors, such as long distances from continental seismic networks and strong noise interference. Therefore, it has been difficult to establish a good correlation between seismicity, waveform characteristics, and geological features on the seafloor, such as fracture zones (FZs), seamounts, and inactive ridges.

Recent developments and advancements in broadband ocean-bottom seismometer (OBS) technology have enabled long-term observations on the seafloor (e.g., Suetsugu and Shiobara, 2014; Sumy et al., 2015; Stähler et al., 2016; Barchek et al., 2020; Shiobara et al., 2021; Eilon et al., 2022), allowing the detection and location of small earthquakes ($M < 3$) that were previously undetectable (e.g., Begnaud and Stakes, 2000; Tréhu et al., 2018). Using OBS data, the seismicity in various tectonic settings in the oceanic environment, such as intraplate regions (e.g., Guo et al., 2022), subduction zones (e.g., Bie et al., 2020; Eimer et al., 2020), ridges (e.g., Shen, 2002), and seamount volcanic regions (e.g., Levy et al., 2018) has been examined. In 2018, a South Korea–Japan research collaboration, which is a part of the Pacific array initiative project (Kawakatsu and Utada, 2017; see Data and Resources) began. The primary goal of this project was to provide geophysical constraints on the structure of the lithosphere–asthenosphere system and the geodynamic evolution beneath the oldest Pacific from the array equipped with broadband OBSs and ocean-bottom electromagnetometers, entitled “Oldest-1 array” (Fig. 1). The Oldest-1 array provided high-quality seismic data with low noise from the deep sea (Kawano et al., 2023) from October 2018 to November 2019 (Fig. 1).

In this study, we detected and located seismic events at local-to-regional distances (reaching ~700 km from the array center) that were not previously reported in global earthquake catalogs, such as those from the International Seismological Center and National Earthquake Information Center, during the Oldest-1 array observational period. The observed earthquake locations and waveform characteristics show good correlation with geologic features such as knolls and seamounts; several epicenters are positioned collinearly with the FZ. In addition, we investigated waveform similarity, event relocation, and T -phase observations to identify the event characteristics and the role of seamounts.

Data and Methods

Data acquisition and quality

We retrieved data from the Oldest-1 array, consisting of 11 broadband ocean-bottom seismometers (BBOBSs) and 12

differential pressure gauges (DPGs) (Fig. 1). The Oldest-1 array (OL01–OL12) was deployed in the oldest part of the Pacific (160–180 Ma), with water depths ranging from 5609 to 6033 m (Table 1), and data were continuously recorded from October 2018 to November 2019. The BBOBSs were equipped with CMG-3T broadband seismometers (Guralp Systems Ltd.) and DPGs (NiGk Corporation), operating at a sampling rate of 100 samples per second. BBOBS at OL12 failed to record data. The data were corrected for tilt and compliance noise in the vertical component to minimize the interference from the horizontal and pressure components (Kawano et al., 2023).

As shown in Kim et al. (2023), describing background noise of each site, significant noise reduction was observed within the noise notch frequency band (0.01–0.05 Hz) and short-period range (2–25 Hz). Furthermore, the short-period noise levels within the array were notably lower (by ~50 dB) than those from nearby island stations. Despite the seasonal variation induced by wind-generated ocean surface waves in the short-period range, noise levels remained lower than those of the microseism band (0.05–0.5 Hz). Based on the probabilistic power spectral density (McNamara and Buland, 2004) of the Oldest-1 array data (Kim et al., 2023), we selected the optimal frequency band for earthquake detection as the 5–20 Hz band to mitigate microseism noise and enhance the detection of small earthquakes at local and regional distances.

Seismic event detection

We probed for possible earthquake signals using an amplitude-based method based on the short-term average over the long-term average (STA/LTA; Allen, 1978). This method has been widely used in environments where no prior information regarding the earthquake source is available. To increase the computational efficiency, we used the recursive STA/LTA method proposed by Withers et al. (1998) as follows:

$$\text{STA}_i = C_{\text{STA}}x_i + (1 - C_{\text{STA}})\text{STA}_{i-1}, \quad (1)$$

$$\text{LTA}_i = C_{\text{LTA}}x_i + (1 - C_{\text{LTA}})\text{LTA}_{i-1}, \quad (2)$$

in which x represents the data; i denotes the time index; and C_{STA} and C_{LTA} are $1/N_{\text{STA}}$ and $1/N_{\text{LTA}}$, respectively; N_{STA} and N_{LTA} are the numbers of samples in the STA and LTA windows, respectively. The STA and LTA windows were set to 0.5 and 60 s, respectively, which are commonly used initial values (Trnkoczy, 2009). This method was applied to continuous vertical-component waveforms from October 2018 to November 2019, which were filtered at 5 and 20 Hz. The signals were declared as possible earthquakes when the STA/LTA exceeded five and when more than four stations were triggered. Once declared, the P - and S -wave arrival times were picked by visual inspection.

We also employed a template matching method based on waveform similarity to detect additional events (e.g., Kim, 2013; Ross et al., 2019). Events detected using the STA/LTA

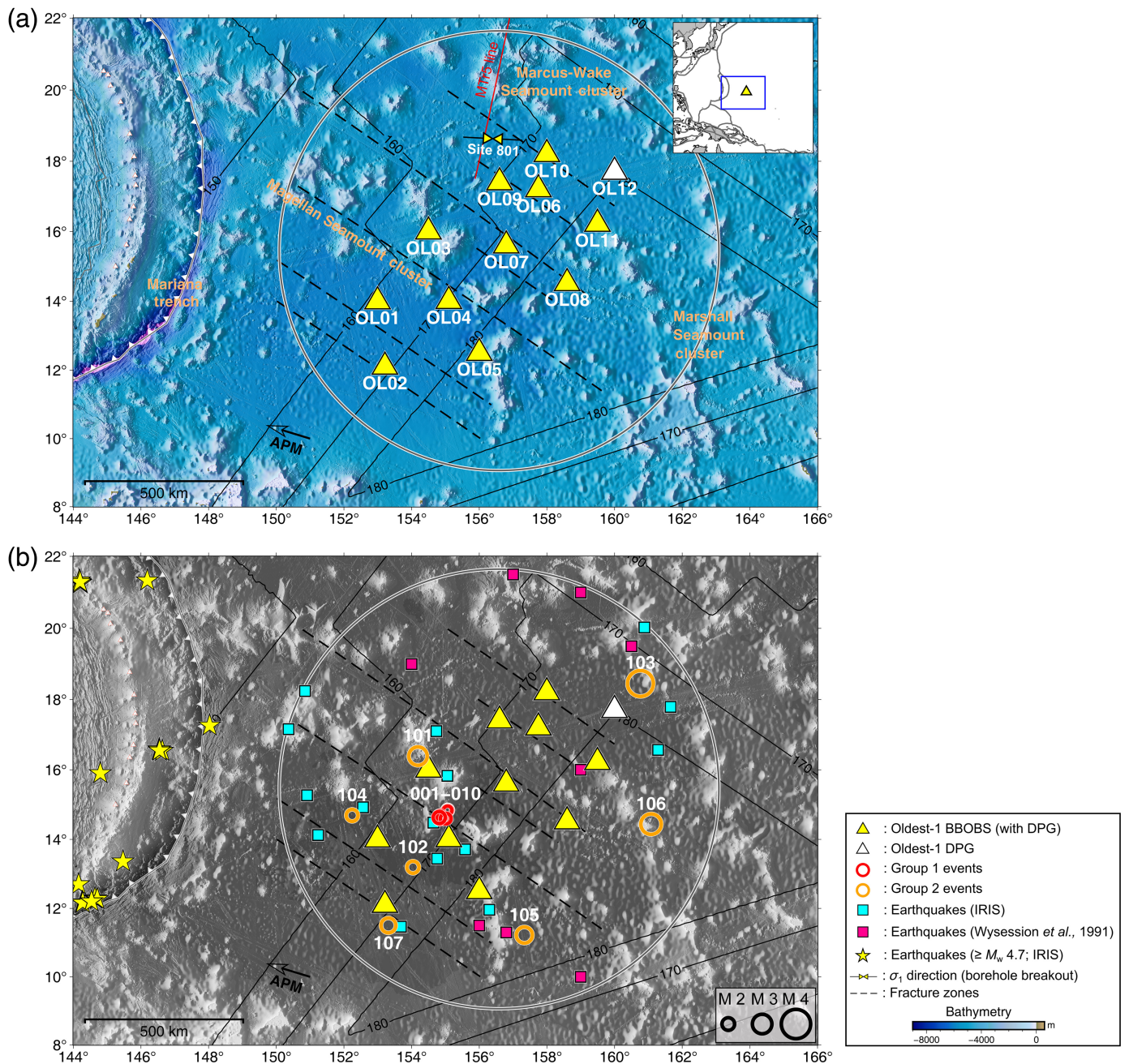


Figure 1. Map showing the Oldest-1 array and seismic activity. (a) Seismic array geometry and geological features. Our study area is within a 700 km radius of the array center (light gray circle). Eleven three-component broadband ocean-bottom seismometers (BBOBSs) equipped with differential pressure gauges (DPGs) are shown as green triangles, with the open triangle indicating a station that recorded DPG data only. Fracture zones (FZs), indicated by dashed lines, are defined by geomagnetic reversal patterns (Nakanishi et al., 1992) and seismic profiling (Abrams et al., 1992). The red thin line indicates MTr5 seismic survey line (Kaneda et al., 2010). Ocean drilling program (ODP) site 801 of leg 129 (Abrams et al., 1992) is situated north of the station OL09, and its principal stress direction (Heidbach et al., 2016) is indicated. An open arrow indicates the direction of current absolute plate motion (APM) (Beavan et al., 2002). Plate

boundaries and ages are obtained from Bird (2003) and Müller et al. (2019), respectively. Bathymetry data were obtained from General Bathymetric Chart of the Oceans (GEBCO) Compilation Group (2019). The upper-right inset shows the study area and location of the seismic array. (b) Locations of earthquakes detected by the Oldest-1 array (red and orange circles, scaled by earthquake magnitude). The white text indicates event IDs (Table 1). The cyan and magenta squares represent earthquakes reported by global earthquake catalog of Incorporated Research Institutions for Seismology (IRIS) and Wysession et al. (1991), respectively. The yellow stars indicate events reported by Global Centroid Moment Tensor (Global CMT) project during our observation period. The color version of this figure is available only in the electronic edition.

TABLE 1
List of Broadband Ocean-Bottom Seismometers (BBOBSs) of the Oldest-1 Array

Station ID	Latitude (°N)	Longitude (°E)	Depth (m)
OL01	13.9919	152.9931	5960
OL02	12.0983	153.2105	5934
OL03	15.9993	154.4987	5687
OL04	14.0012	155.0994	6033
OL05	12.4975	155.9999	5942
OL06	17.2014	157.7493	5790
OL07	15.5995	156.7986	5974
OL08	14.5171	158.5977	5765
OL09	17.3999	156.6010	5755
OL10	18.1993	157.9982	5684
OL11	16.2178	159.4947	5766
OL12*	17.6992	159.9983	5609

*Only differential pressure gauge (DPG) is available.

method were used as templates. The template window was set to 5 s before and 30–120 s after the *P*-wave arrival, including most of the *P*- and *S*-wave coda, depending on the event–station distance. The correlation coefficient (*C_c*) was calculated by cross correlating the template with all available waveforms. We retrieved matched signals where *C_c* exceeded 0.3 at the four stations closest to the event.

Initially, more than 20,000 events were identified as candidate seismic signals during the Oldest-1 observational period. However, most of the detected signals were transient noise, repeated detections of the same events, or earthquakes located near a trench, primarily the Mariana trench, ~900 km west of the array center (Fig. 1). After manual screening of the detected signals, only 31 events remained as possible earthquakes that occurred within the study region. Among these 31 events, 14 were unlocatable because of the small number of stations that recorded signals (fewer than four). The remaining 17 events were located.

The spectrograms of the 17 events were examined to determine whether they were true seismic signals. Noise signals in a spectrogram typically appear as continuous-amplitude signals over time, differing from the pattern of true earthquake signals (e.g., Webb, 1998). In contrast, earthquake signals have an impulsive onset, showing a distinct peak amplitude and a clear separation of *P*- and *S*-wave arrivals. Figure 2 shows examples of the spectrograms of three detected events compared with one earthquake recorded in the global catalog (the 22 July 2019 M_w 5 event that occurred near the trench). The spectrogram of the 2019 M_w 5 event shows impulsive *P*- and *S*-wave arrival onsets at ~55 and 150 s, respectively (Fig. 2a). The

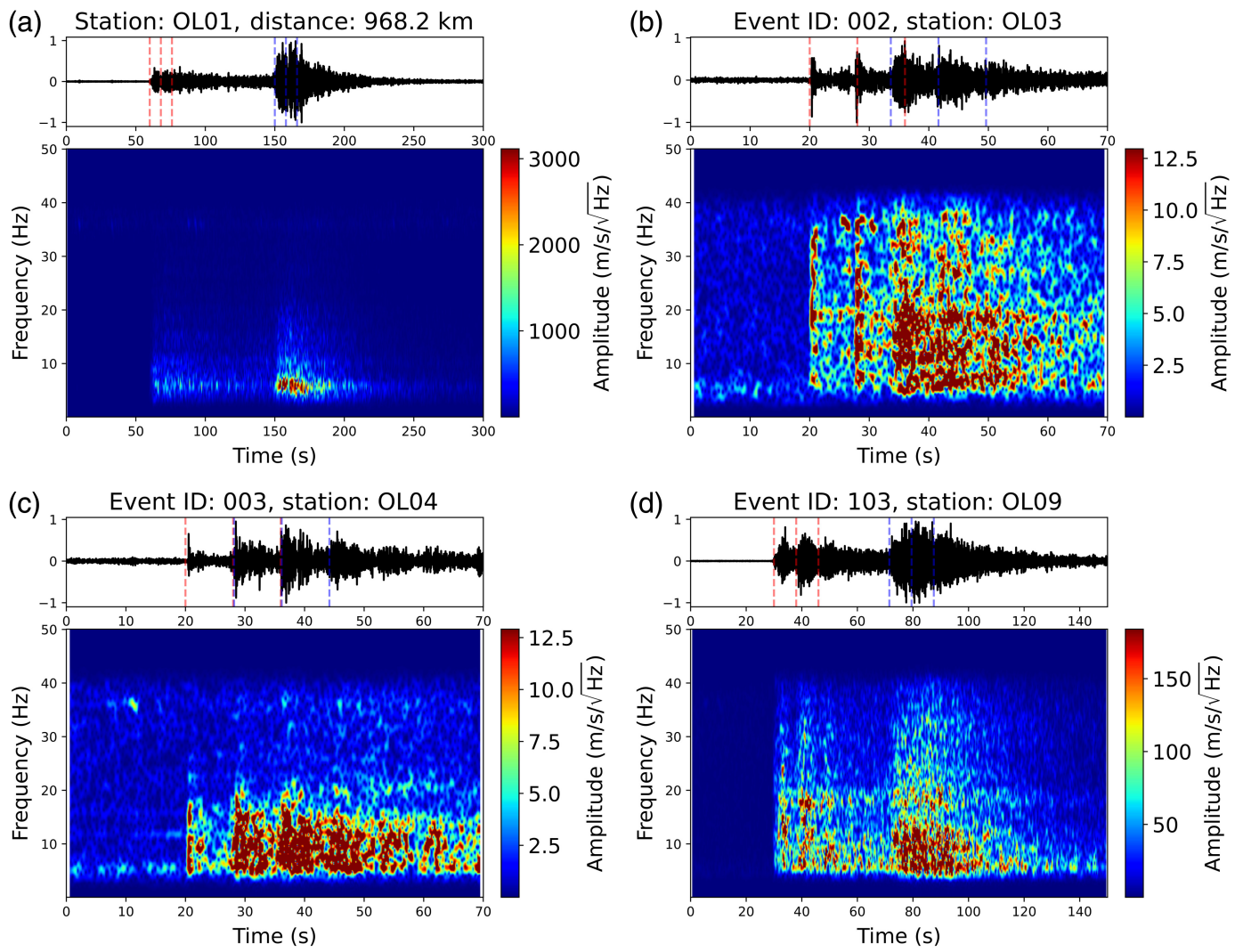
spectrograms of the three detected events also exhibited clear onsets without continuous noise signals over time (Fig. 2b–d).

Earthquake location procedure

Velocity model construction. Seismic velocities higher than those in the Preliminary Reference Earth Model (PREM; Dziewonski and Anderson, 1981) have been found in older parts of the Pacific plate (Maggi *et al.*, 2006). However, because there is no known local velocity model for the study region, we initially used the PREM as a baseline velocity model for the location. We measured arrival-time difference (Δt) between observed and theoretical *P*-wave arrival times for earthquakes near the Mariana trench (reported in the global catalog during the observation period; see Fig. 1b) to validate the velocity model. The measured average Δt was –4.72 s over 150 travel-time measurements (Fig. 3a). This indicates that the PREM predicts velocities to be significantly slower than those actually present in the study region.

To resolve this issue, we adopted a hybrid velocity model (Table S1, available in the supplemental material to this article) constructed by integrating models reported in several previous studies. First, for the oceanic crust, we used the model from the seismic survey that ran a 910 km line with 180 OBSs (line MTr5; Kaneda *et al.*, 2010), deployed north of the Oldest-1 array (Fig. 1a). This line was segmented into three parts: the southern basin, seamount chain, and northern basin. We used the southern basin segment closest to the Oldest-1 array, which can potentially represent oceanic crust, to define the crustal layers of our hybrid model. Specifically, we set the thicknesses of the sediment, upper crust, and lower crust layers to 0.5, 2, and 5 km, respectively. *P*-wave velocities (V_p) range from 1.6 to 2.5 km/s for the sediment layer, 4.5 to 6.6 km/s for the upper crust, and 6.9 to 7.2 km/s for the lower crust (Kaneda *et al.*, 2010). *S*-wave velocity (V_s) was defined as V_p divided by 1.79 and 1.82 for the upper and lower crust, respectively, which are derived from a seismic survey on the 129 Ma-old Pacific plate near WP-2 (Shinohara *et al.*, 2008). Second, for mantle V_p and V_s , we used a 0.5% higher velocity for the lithospheric mantle based on the model by Shinohara *et al.* (2008). The V_p adjustment yielded the smallest average *P*-wave arrival-time difference (Fig. 3a). Below the lithospheric mantle, we used the PAC06 model (Tan and Helmberger, 2007), which was constructed based on the differential travel times of multibounce *S*-wave through the Pacific plate with ages of 10–125 Ma. V_p/V_s for the mantle was set to 1.73 (Shinohara *et al.*, 2008).

Earthquake location and relocation. To locate the 17 events, we utilized arrival-time picks and the *BayesLoc* program to estimate the joint probability of event locations through Bayesian probabilistic realization (Myers *et al.*, 2007, 2009). In total, 232 arrival-time picks, comprising 113 *P* and 119 *S* wave-picks were used at the event locations (Fig. S1). Given the data quality and sparse coverage due to the small number of stations,



the focal depth was fixed to the crustal depth. Prior to fixing a depth, we verified a range of 2000 event depth samples from Bayesian realization results (Fig. S2). Because the average depths of all events were between 3 and 5 km, we fixed the focal depth fixed at 4 km. The location and uncertainty of each event were determined using 2000 samples at a fixed focal depth of 4 km (Fig. S3). The average horizontal uncertainties of 4 km and other fixed focal depths were found to be in the range of 6.6–7.0 km (Fig. S4).

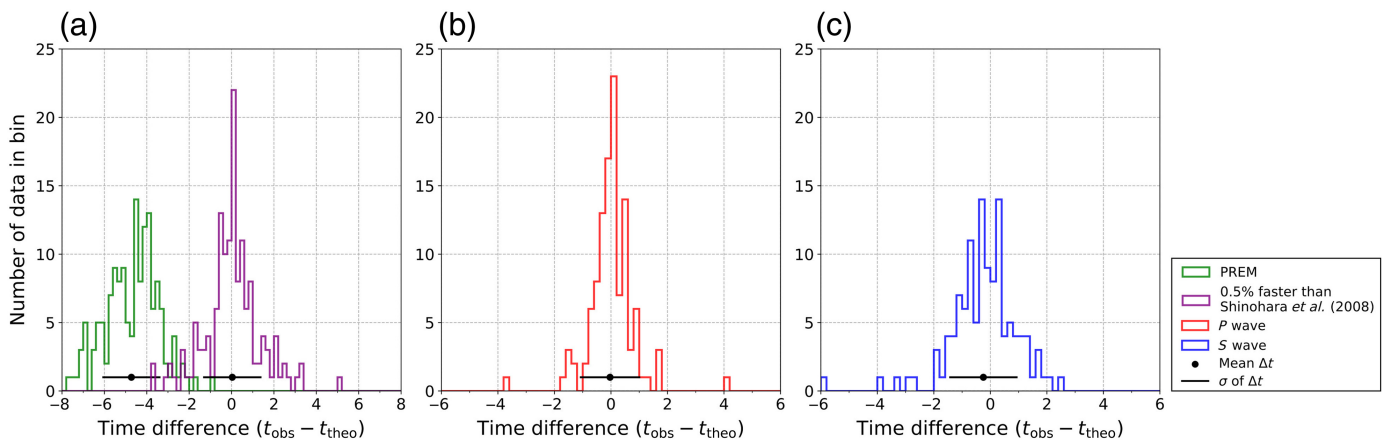
Next, we applied the double-difference relocation method (Waldhauser and Ellsworth, 2000), known as *hypoDD*, to five closely located events. This method is used to enhance location precision and can be quite useful for retrieving any lineament in geological structures, such as a fault trace. Differential travel times (dt) were used to determine relative locations using the singular vector decomposition (SVD) method (Waldhauser, 2001). Relocation was performed using the following dt datasets: (1) phase data of the P - and S -wave arrivals used in location and (2) data filtered at 5–20 Hz and corrected using the waveform cross-correlation (WCC) technique to reduce arrival-time-picking errors (e.g., Schaff and Waldhauser,

Figure 2. Examples of spectrograms for (a) an earthquake recorded in the global catalog (M_w 5; origin time: 22 July 2019 04:52:41; latitude: 12.17° N; longitude: 144.26° E), and (b–d) detected events in this study. The first red and blue dashed lines represent P - and S -wave arrivals, respectively. The lines following P - and S -wave arrivals indicate two theoretical water reverberation phases, D_w/V_w , in which D_w and V_w are water depth (6 km) and velocity in water (1.5 km/s), respectively. The color version of this figure is available only in the electronic edition.

2005). In the WCC, the window was set from 1 s before to 2 s after the P - and S -wave arrival times. Data with a Cc value exceeding 0.7 were collected, and the Cc value for an individual event was used as a weighting factor in the relocation. A total of 136 dt for the five events were used to estimate relocation errors based on SVD.

Magnitude estimation

Because there was no local attenuation information in our study region and the detected events had a low signal-to-noise ratio (SNR) in the low-frequency range, we used the regional



body-wave magnitude scale, $m_b(Sn)$, to estimate the magnitude of the detected events in the high-frequency range (Kim et al., 2020). We measured the Sn peak amplitude (A) in nanometers (nm) for a time window centered on a theoretically calculated Sn pick for SNRs larger than two. We used the waveform of vertical component filtered at 5–10 Hz within a window length (T) based on distance (Δ). The window length was determined as follows:

$$T(\Delta) = 2 \times T_p \times \left(\frac{\Delta}{\Delta_p} \right), \quad (3)$$

in which T_p is a time window length of 15 s; and Δ_p is a distance of 1000 km. The $m_b(Sn)$ was determined using the following equation (Kim et al., 2020):

$$m_b(Sn)_{ij} = \log_{10}(A_{ij}) \text{(nm)} - 2.18 \log_{10}\left(\frac{100}{\Delta_{ij}}\right) \text{(km)} + 1.34, \quad (4)$$

in which indices i and j indicate the i th station and the j th event, respectively; Δ_{ij} is the distance from the j th event to the i th station; and $m_b(Sn)_{ij}$ is the station magnitude. The $m_b(Sn)_j$ values were obtained by averaging the $m_b(Sn)_{ij}$ values measured at each station.

Results

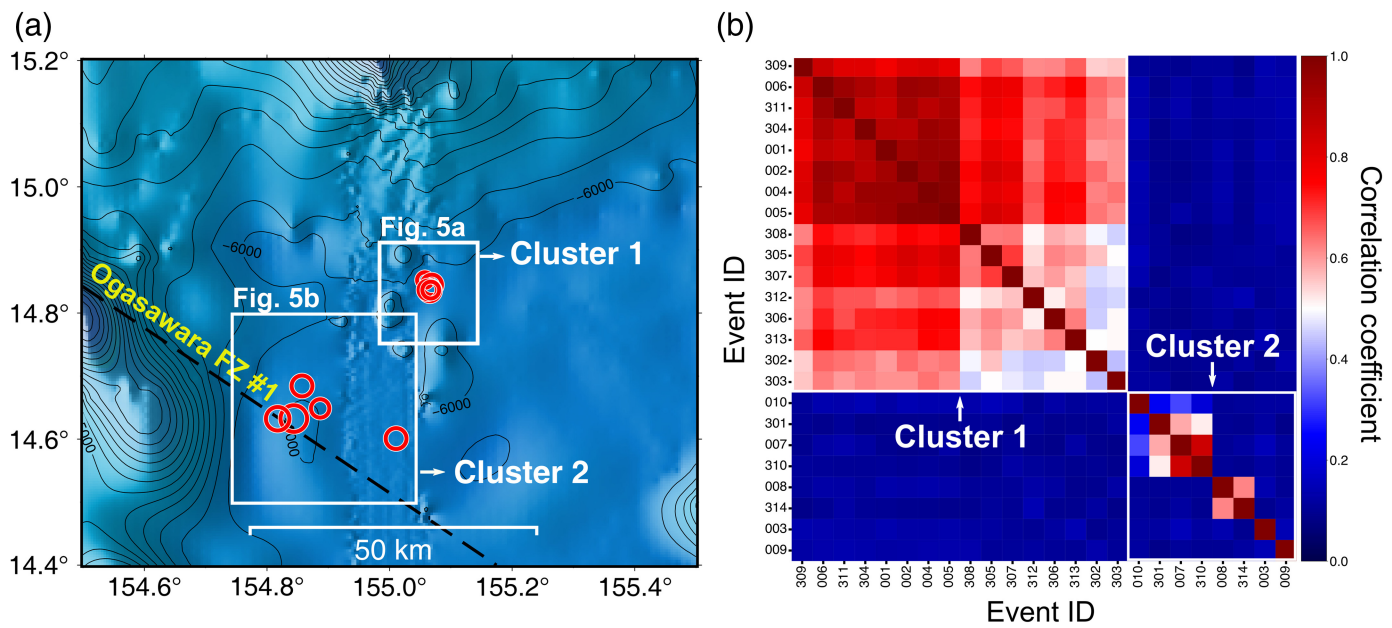
We located 17 earthquakes with $m_b(Sn)$ of 0.9–3.7 (Fig. 1b). Their Δt values for P - and S -wave arrivals are -0.03 ± 1.03 s and -0.08 ± 1.14 s, respectively (Fig. 3b,c). Because the event locations were widely distributed in the study region, we grouped the 17 events into two groups based on their spatial proximity to investigate any correlation between geologic features and earthquakes. The ten events of the first group (Group 1) were located ~ 80 km north of station OL04 within a 50×50 km 2 area (Fig. 4a). Group 1 included 14 unlocatable events (Fig. 4b). In contrast, the seven events of the second group (Group 2) were located periphery of the array and farther from each other (Fig. 1b).

Figure 3. Histogram showing measured arrival-time differences between observed and theoretical travel-time data denoted as Δt . (a) The Δt for the P wave of earthquakes reported by IRIS during the observation period (Fig. 1b). Theoretical travel times are calculated using both the Preliminary Reference Earth Model (PREM; Dziewonski and Anderson, 1981) and a hybrid model with a 0.5% faster lithospheric mantle used in this study. The black dots and horizontal lines represent average Δt and standard deviation (σ), respectively. The averaged Δt values are -4.72 and 0.03 s for PREM and the 0.5% faster hybrid model, respectively, whereas the σ of Δt is 1.33 and 1.33 s for P and S waves, respectively. A bin size is set to 0.2 s, and a total of 146 arrival times are used to estimate Δt . (b,c) The Δt for P and S waves of the 17 events obtained from the 0.5% faster hybrid model, respectively. The averaged Δt are -0.06 and -0.14 s for P and S waves, respectively, whereas σ is 1.03 and 1.14 s for P and S waves, respectively. A total of 232 arrival times are used to estimate Δt . The color version of this figure is available only in the electronic edition.

Earthquakes in Group 1

The ten events in Group 1 (event IDs 001–010; Table 2) ranged in magnitude from 0.9 to 2.2 . The numbers of arrival-time picks for P - and S -wave arrivals are 45 and 49 , respectively, with the Δt values of 0.11 ± 0.25 s for P waves and -0.33 ± 0.55 s for S waves. Their average major and minor horizontal location uncertainties are 2.95 ± 0.3 km and 2.2 ± 0.2 km, respectively (Table 2, Fig. 5a,b). Although the magnitudes of the Group 1 events were small, the relatively high station azimuthal coverage ($\sim 110^\circ$) and presence of one close station (OL04, within an average distance of ~ 84 km from the events in Group 1) provided reliable arrival-time picks, leading to reduced location uncertainty.

Because the events in Group 1 were located in two different areas, specifically the northeast and southwest regions (Fig. 4a), we further divided Group 1 into two clusters. The five events (event IDs 001, 002, and 004–006; Cluster 1) were located close to each other and had high waveform similarity (Figs. 4b and 6a–c); therefore, these events were relocated. Figure 6d shows the relocation results for ten connected event pairs and errors within an 80×80 m 2 area. They have an average horizontal



error of less than 1 m and a root mean square (rms) residual time of less than 0.001 s. Although the earthquake locations did not show lineament, we found that Cluster 1 events occurred adjacent to a geologic feature, specifically 200–300 m high knolls, within the epicentral uncertainty range (Fig. 5a).

However, the five events in Cluster 2 (event IDs 003 and 007–010) were not relocated because of their low waveform similarity and large distances between the events (Fig. 4b). Nevertheless, they were situated along Ogasawara fracture zone (OFZ) #1 (Abrams *et al.*, 1992). The average distance from the OFZ was ~12 km (Fig. 5b).

Earthquakes in Group 2

The magnitudes of the seven events in Group 2 (event IDs 101–107) range from 1.9 to 3.7. The number of time picks for *P*- and *S*-wave arrivals are 68 and 70, respectively, with Δt values recorded at -0.13 ± 1.31 s for *P* waves and -0.19 ± 1.46 s for *S* waves. Their average major and minor horizontal uncertainties are 5.5 ± 1.7 km and 3.2 ± 0.9 km, respectively (Table 2, Fig. 5c–i). Although the lower azimuthal coverage and greater event–station distances contributed to larger location uncertainties compared with those for events in Group 1, relatively large magnitudes with more arrival-time picks (Fig. S1) allowed us to determine the epicentral locations. The epicenters of the four events (event IDs 102, 104, 105, and 107) were located on the abyssal plain with no recognizable geologic features (Fig. 5d,f,g,j). However, the other three events (event IDs 101, 103, and 106) were located adjacent to seamounts (Fig. 5c,e,g).

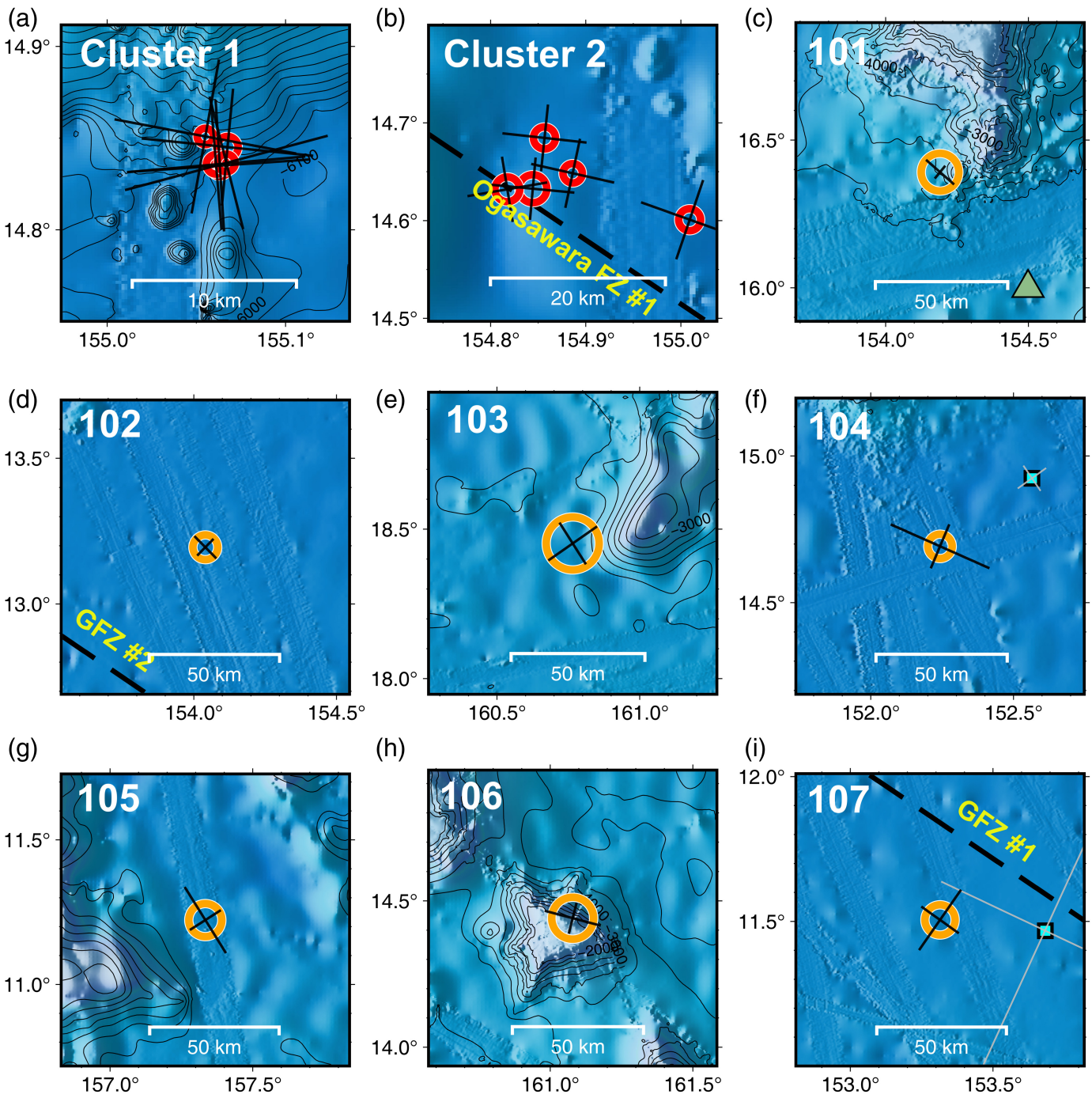
T-phase observation in three earthquakes in Group 2

Seamounts that rise above a critical depth of ~4.5 km from the sea surface can facilitate the excitation of the *T* phase by providing an efficient path to the sound fixing and ranging (SOFAR)

Figure 4. (a) Map showing locations of ten events of Group 1. These events are grouped into clusters 1 and 2 (Table 1; see Fig. 5a,b). (b) Correlation coefficient (Cc) matrix of 24 event pairs reordered by hierarchical clustering. The ten events (with event ID starting from 001 to 010) are located, whereas the 14 events (from 301 to 314) are only detected. The Cc values is calculated for data recorded at station OL04 (Fig. 1b). The time window is set at 2 s before and 35 s after the *P*-wave arrival. The Cc matrix illustrates at least two distinct clusters, denoted as Cluster 1 and 2. Cluster 1 events exhibit high waveform similarity (see Fig. 6); the Cc values of Cluster 2 events are low. The color version of this figure is available only in the electronic edition.

channel. Below this critical depth, the *T* phase is strongly attenuated (Williams *et al.*, 2006). Therefore, the presence of the *T* phase is indicative of the spatial proximity between the seismic event and the seamount, suggesting that the seamount plays a crucial role in the transmission of these signals.

To identify the *T* phase from the waveform at each station, we first manually determined a start time of the *T*-phase window within ± 20 s, based on the group velocity of the *T* phase, which is ~ 1.5 km/s. Next, stations within 150 km of the events were excluded to avoid the influence of the *S*-wave coda. In addition, we excluded stations that measured no *T*-phase signal. We observed a clear *T* phase in the waveforms of three events (event IDs 101, 103, and 106) (Fig. 7a–f). Stations OL03 and OL12 (within 150 km) were excluded for event IDs 101 and 103, respectively. We also excluded two stations (OL02 and OL03) for event ID 103, and seven stations (OL01, OL03, OL04, OL06, OL09, OL10, and OL11) for event ID 106 because they showed no *T*-phase signals. The epicenters of event IDs 101, 103, and 106 were located adjacent to seamounts (Fig. 5c,e,h) and situated at water depths of 3.5, 5.3, and 1.1 km (Fig. 7g), respectively. In contrast, no *T* phase



was observed in the other events in groups 1 and 2, epicenters for which were situated on the abyssal plane at depths greater than 5.7 km (Fig. 7g).

We further estimated the rms SNR of the T phase from DPG data filtered in the 5–20 Hz range. Because the T -phase amplitude is less affected by the focal mechanism and depth of an event, but is proportional to the magnitude (De Caro *et al.*, 2020), we normalized the T -phase signal by the P -wave signal to remove the magnitude difference. We set the signal window to 10 s before and 60 s after the T -phase arrival, and the noise window was defined from 8.5 to 5.5 km/s to include P -wave energy. Figure 7h shows the T -phase SNR for the three events

Figure 5. Maps showing 17 event locations (circles) and horizontal uncertainties (black crosses). (a,b) Events within clusters 1 and 2. (c–i) Events in Group 2 (event ID of 101–107). The cyan squares with gray crosses represent events with their horizontal uncertainties reported by global catalog. The black dashed lines in panel (b) represent the Ogasawara fracture zone (OFZ) in seismic profiling (Abrams *et al.*, 1992); black dashed lines in panels (d) and (e) represent the FZ determined by geomagnetic reversal patterns (denoted as GFZ) (Nakanishi *et al.*, 1992). The black thin lines indicate 50 m bathymetry contour lines in panel (a); the others are 500 m contours. The color version of this figure is available only in the electronic edition.

TABLE 2
List of 17 Earthquakes Detected by the Oldest-1 Array

Event ID*	Origin Time (yyyy/mm/dd hh:mm:ss.s)	Latitude (°)	Longitude (°)	Magnitude m_b (Sn)	Major Axis (km) [†]	Minor Axis (km) [†]	Major Axis Angle (°) [‡]
001 ^a	2019/05/21 16:37:30.5	14.8509	155.0551	0.9	3.1	2.6	172.7
002 ^a	2019/06/12 11:11:25.8	14.8451	155.0675	1.6	3.0	1.9	175.1
003 ^b	2019/06/18 01:34:04.9	14.6846	154.8566	1.6	2.7	2.1	173.9
004 ^a	2019/07/01 06:14:33.0	14.8350	155.0632	1.6	3.1	2.2	5.5
005 ^a	2019/07/01 06:56:04.1	14.8357	155.0611	1.4	3.1	2.1	4.6
006 ^a	2019/07/29 02:56:03.7	14.8365	155.0668	1.1	3.4	2.3	13.4
007 ^b	2019/08/23 19:23:09.6	14.6326	154.8443	2.2	2.6	1.9	176.6
008 ^b	2019/08/29 17:49:22.6	14.6484	154.8863	1.3	2.7	2.2	165.6
009 ^b	2019/09/08 18:50:17.5	14.6009	155.0093	1.6	3.1	2.5	164.6
010 ^b	2019/10/27 13:51:57.4	14.6320	154.8176	1.9	2.6	2.1	11.6
101	2019/03/11 01:03:33.7	16.3914	154.1905	2.9	3.7	1.7	140.1
102	2019/04/01 00:07:05.8	13.1948	154.0404	1.9	2.9	2.3	136.8
103	2019/06/26 23:39:51.5	18.4523	160.7653	3.7	5.0	4.4	34.7
104	2019/08/02 01:49:50.1	14.6921	152.2427	1.9	8.4	4.1	149.5
105	2019/08/16 22:06:59.5	11.2227	157.3339	2.6	6.3	3.0	121.9
106	2019/08/31 06:25:53.2	14.4407	161.0788	3.1	5.7	3.0	164.0
107	2019/10/07 05:19:52.9	11.5051	153.3144	2.4	6.5	4.0	55.5

Origin time, location, and horizontal uncertainties are from *BayesLoc* location (Myers et al., 2007, 2009).

*Events are categorized into two groups. Events in Group 1 are denoted from 0, and events in Group 2 from 1. Within each group, events are arranged in an ascending order based on their origin times. Superscript a indicates event ID indicates Cluster 1 in Group 1; superscript b indicates event ID indicates Cluster 2 in Group 1.

[†]Major and minor axes represent one standard deviation of sample distributions of *BayesLoc* realization.

[‡]Angles are measured counterclockwise from the east.

plotted against water depth. Specifically, event IDs 101, 103, and 106 have SNRs of 0.96 ± 0.35 , 0.73 ± 0.37 , and 1.14 ± 0.32 , respectively. These results reveal an inverse relationship between T -phase amplitude and water depth at the epicenter (Fig. 7h), indicating that T -phase excitation is influenced by the water depth, which corresponds to the seamount height.

Discussion

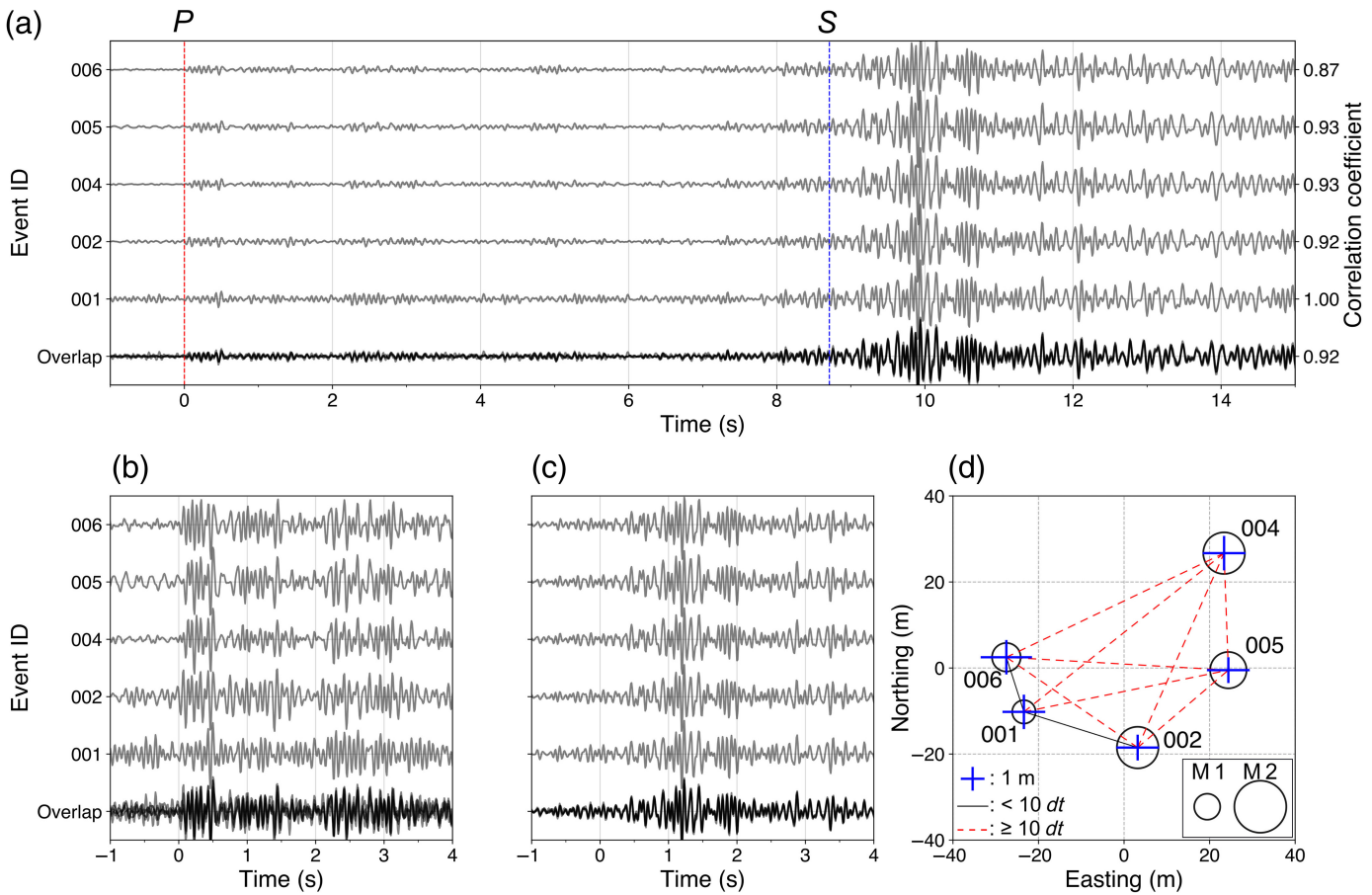
As many previous studies have reported, intraplate seismicity typically occurs in areas with pre-existing weaknesses. For example, Schulte and Mooney (2005) suggested a correlation between seismicity and ancient rifts based on an earthquake catalog for magnitudes larger than 4.5 in the stable continental region. Okal (1984) proposed a correlation between oceanic intraplate earthquakes with magnitudes larger than 4.7 on the southern Pacific plate and major seamounts, ridges, or FZs. Bergman and Solomon (1980, 1992) reported earthquakes with magnitudes larger than 4.7 and suggested that these earthquakes are likely to occur near the FZs. However, Wysession et al. (1991) concluded that approximately half of the earthquakes reported during 1913–1988, previously determined

to be oceanic intraplate earthquakes, were not true intraplate seismic events over the Pacific basin. They reported that many of the events in the Pacific basin were interplate events or nuclear explosions. This indicates that many of the oceanic intraplate earthquakes in the previously reported catalogs suffered from large horizontal uncertainties ($\sim 15\text{--}50$ km) because of the large distances between events and low station coverage.

In this study, utilizing the Oldest-1 array data, we substantially improved the location accuracy for oceanic intraplate earthquakes, such that most of the events in our catalog were located adjacent to actual geologic features (Fig. 5a–c,e,h). The average horizontal uncertainty of the 17 events was 3.2 km, and this estimate was nearly 5–15 times better than those in previous catalogs. However, similar to previous studies, we were unable to determine the focal depths and mechanisms because of limited station geometry and datasets. This implies that ambiguities remain in the spatial correlation, particularly for oceanic plates.

Epicenters correlated to geologic features

Cluster 2 event proximity to FZs. The mechanical strength of the FZs can be weakened by alteration and increased pore



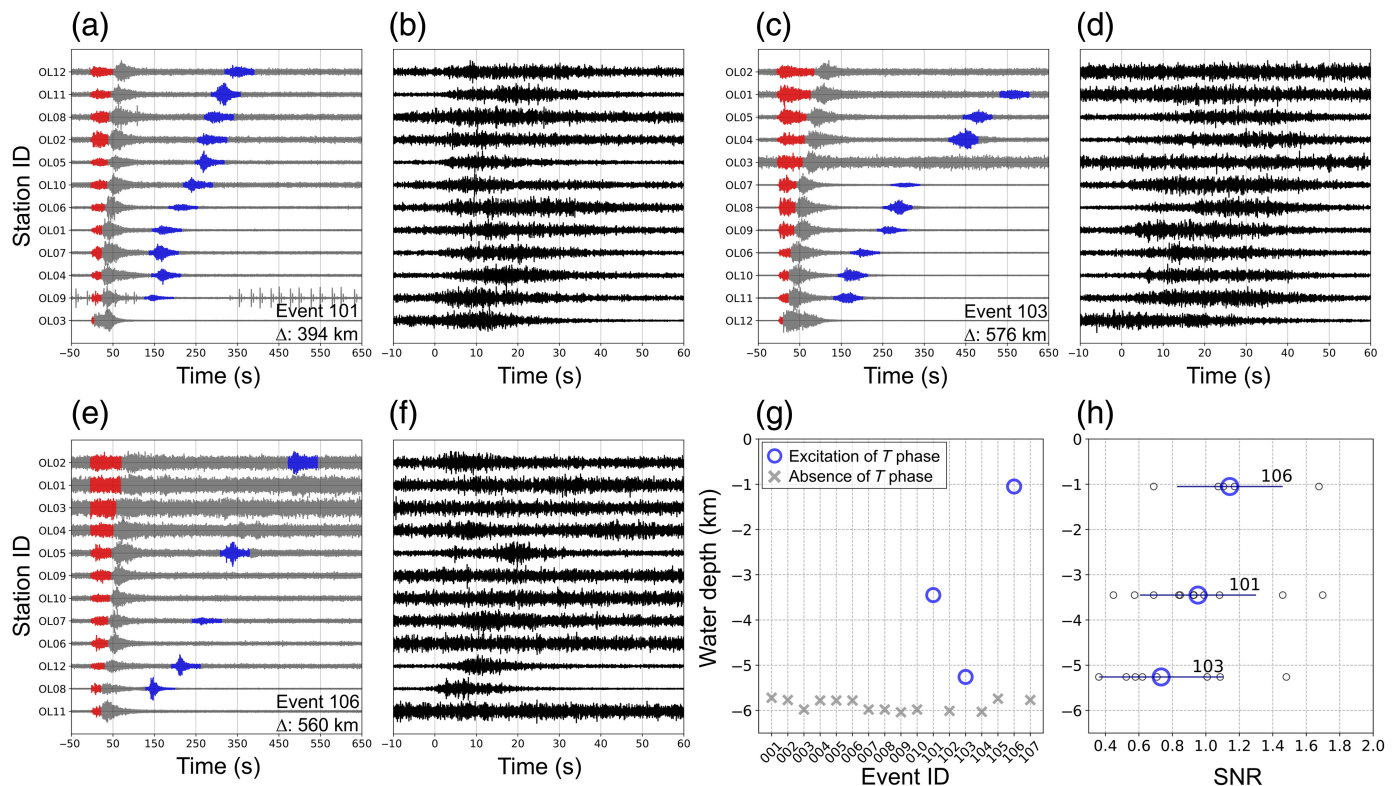
pressure owing to water circulation during their formation (e.g., Morrow *et al.*, 2019). Weakened FZs may have contributed to the formation of seamounts by providing a path for volcanic activity (Lowrie *et al.*, 1986). In our study region, Abrams *et al.* (1992) suggested that the OFZs may have been a focal point for generating midplate volcanism (Magellan Seamount Chain; see Fig. 1) from the Aptian (~121 Ma) to the Santonian (~84 Ma), indicating that the OFZs could potentially be a pre-existing weak zone. The epicenters of Cluster 2 located along OFZ number 1 indicate that the FZ may be seismically active, regardless of its age (Figs. 4a and 5b).

We were able to detect earthquakes only along OFZ #1, but not along other FZs, during our one-year OBS deployment period (Fig. 1). This could be primarily due to the detection limit of our array and/or the short observation period for detecting events in the FZs, which could have low strain rates (Kreemer *et al.*, 2014). However, we cannot exclude the possibility that the mechanical strength of these FZs is as strong as that of the undisturbed lithosphere (e.g., Sandwell, 1984; Wessel and Haxby, 1990; Bergman and Solomon, 1992). Hence, further long-term seismic observations are necessary to investigate the seismic activity at the FZs in the oldest Pacific.

Earthquake proximity to seamounts and knolls. During the one-year observation period, we observed three events in Group 2 that occurred near seamounts (Fig. 5c,e,h) and five

Figure 6. (a) Waveform similarity of five relocated events in Cluster 1. The time window is set from 1 s before to 15 s after the P-wave arrival, and all waveforms are filtered at 5–20 Hz. Each row represents a waveform of an individual event, with the final row displaying their overlapped waveforms. Ccs with respect to event 001 are presented at the end of each trace. (b,c) Waveforms within 1 s before and 4 s after the P- and S-wave arrival times, respectively. (d) Results showing the relocated earthquakes and connectivity for ten event pairs of the five events at the final iteration for the relocation. Event pairs are color coded to indicate how many station differential times (dt) are used in each event pair (red dashed line indicating $\geq 10 dt$ and black solid line $\leq 9 dt$). The blue crosses show 95% formal error of relocation calculated from the singular vector decomposition (SVD) used in hypoDD (Waldhauser, 2001) and are exaggerated by a factor of five. The color version of this figure is available only in the electronic edition.

events in Cluster 1 near 200–300 m high knolls (Fig. 5a), which could be associated with the reactivation of pre-existing faults near such geologic features. Several studies have suggested that stresses caused by volcanic loading can lead to faulting around volcanic islands. For instance, McGovern (2007) suggested that the M_w 6.7 and 6.5 earthquakes that occurred in the Big Island of Hawaii were both caused by stress due to volcanic loading. In addition, Klein (2016) suggested that the cause of numerous earthquakes at the periphery of the Big Island could be caused by volcanic loading based on their P and T axes distributions



aligned with volcanic centers. Although a detailed investigation similar to that shown in previous studies cannot be performed in this study, the seismicity concentrated nearest to the geologic features indicates local deformation, possibly due to loading stress regardless of age (~60–70 Ma; Abrams *et al.*, 1992; Hirano *et al.*, 2008).

Waveform characteristics

Cluster 1: High-waveform similarity and precise relocation. Repeating earthquakes rupture the same fault patch with the same focal mechanism and are characterized by nearly identical waveforms (e.g., Uchida and Bürgmann, 2019). Because dense seismic networks are essential for detecting and characterizing such seismic events, most studies have been conducted in continental regions (e.g., Abercrombie *et al.*, 2020; Waldhauser and Schaff, 2021). Such studies are rare in the oceanic environment; Tréhu *et al.* (2015) reported offshore earthquakes in the Cascadia subduction zone using Cascadia initiative data, which include several repeating earthquakes that occur along the plate boundary. In this study, we found that the five events in Cluster 1 exhibited high-waveform similarity with a Cc exceeding 0.92 (Fig. 6a–c) and were precisely relocated within an $80 \times 80 \text{ m}^2$ region (Fig. 6d). The characteristics of the Cluster 1 events may imply the presence of repeating earthquakes in the oldest Pacific lithosphere.

Group 2: T phase and others. The exact excitation mechanisms of the T phase are not fully understood and can be influenced by factors such as source mechanisms, seafloor

Figure 7. Waveform plots showing T phase in DPG data. (a,b) Event 101 waveforms within the time window from 50 s before to 650 s after the P-wave arrival and T-phase waveforms, respectively. All waveforms are filtered from 5 to 20 Hz. The waveforms are arranged based on their distance from the event, and an average distance (Δ) from each event is indicated in the lower right corner of each figure. The red and blue colored waveforms represent arrivals at velocities of 8.5–5.5 km/s and the period 10 s before to 60 s after the T-phase arrival, respectively. (c–f) Same as panels (a) and (b) but show events 103 and 106, respectively. (g) A plot for water depth (GEBCO Compilation Group, 2019). The blue circles indicate three events with T-phase excitation, and gray crosses indicate events with an absence of T phase. (h) Signal-to-noise ratios (SNRs) for three events with T-phase excitation plotted against the water depth. The SNR is estimated using the root mean square (rms) amplitude of the T phase over the rms amplitude of the P wave at each station. Averaged SNR and standard deviation are denoted by blue circles and horizontal bars, respectively. Estimated SNR for each station is represented by small black circles. The color version of this figure is available only in the electronic edition.

roughness, and sea surface conditions (de Groot-Hedlin and Orcutt, 2001; Dziak, 2001; Godin, 2021). Nonetheless, seamounts can act as radiators that transfer seismic energy to the SOFAR channel (Williams *et al.*, 2006), while also acting as a block (Walker *et al.*, 1992). In this study, we observed a clear T phase in three events in Group 2 located near the seamounts (Fig. 5c,e,h). This indicated that the seamount acted as a radiator. At the same time, two stations for event ID 103 and seven stations for event ID106 showed no T phase (Fig. 7a–f).

The lack of T phase observed at seven stations with event ID 106 could be attributed to its location on the Marshall Seamount cluster (Fig. 1a), in which T -phase propagation may experience strong disturbances with scattering. In contrast, event IDs 101 and 103 were located at the periphery of the Magellan and Marcus Wake seamount clusters (Fig. 1a), respectively, and thus may have encountered less disruption in their paths.

For the other four earthquakes in Group 2, there were no distinct waveform characteristics or spatial correlations with any geologic features on the seafloor. The lack of distinct characteristics in these earthquakes may imply that the seismogenic faults are unrelated to observable geologic features on the seafloor and are likely hidden by the surface cover. These earthquakes primarily occurred in the Pigafetta basins (Fig. 1b), which are covered by Aptian sills and flows (Abrams *et al.*, 1992).

Conclusions

In this study, we presented a one-year intraplate earthquake catalog using Oldest-1 array data on the oldest Pacific plate. This study provided the first detailed seismicity observations at local-to-regional distances in the oldest Pacific lithosphere. A total of 17 earthquakes were identified and categorized into two groups: Group 1 consisted of Cluster 1 with five events and cluster 2 with five events, and Group 2 consisted of seven events. Although we were unable to investigate the focal depths and mechanisms because of data limitations, improved horizontal uncertainties provided the possibility of correlating epicenters with several zones of weakness, such as knolls, FZs, and seamounts.

We also identified the waveform characteristics of the earthquakes. Cluster 1 events, located near knolls exhibited high waveform similarity, and their relocation revealed a small source area. These results indicate that they may share a common source, suggesting the occurrence of repeating earthquakes in oceanic intraplate regions. In contrast, the three events in Group 2 located at shallower water depths near the seamounts exhibited clear T -phase signals. The presence and absence of T -phase excitation revealed that seamount chain complexes could contribute to T -phase propagation. These findings suggest that waveform characteristics are governed by complex interactions among epicenters, paths, and geologic features.

Data and Resources

A description of the Pacific array initiative is available at <http://eri-ndc.eri.u-tokyo.ac.jp/PacificArray/>. Seismograms and differential pressure gauges (DPG) data from the Oldest-1 array were collected by the Seoul National University (SNU) and Earthquake Research Institute (ERI) during the cruise from 26 October to 9 November 2019. The seismic waveform data can be downloaded and are openly accessible from the Ocean Hemisphere Project Data Management Center (OHPDMC; <http://ohpdmc.eri.u-tokyo.ac.jp>). Earthquake catalogs of past seismicity in the oldest part of the Pacific plate (1976–2023) and Mariana trench

(2018–2019) were accessed from the Wilber3 online catalog (<https://ds.iris.edu/wilber3>), Global Centroid Moment Tensor (Global CMT) webpage (<https://www.globalcmt.org>), and International Seismological Centre (ISC) online bulletin (doi: 10.31905/D808B830; <http://isc.ac.uk/iscbulletin/search/catalogue/>). The bathymetry data grid from the General Bathymetric Chart of the Oceans 2019 (GEBCO, doi: 10.5285/836f016a-33be-6ddc-e053-6c86abc0788e) were plotted on a bathymetric map. We utilized ObsPy (<https://docs.obspy.org/>) and the Seismic Analysis Code (<https://ds.iris.edu/ds/nodes/dmc/software/downloads/sac/>) to process the seismic waveforms and Generic Mapping Tools (version 6.4.0.; <https://www.generic-mapping-tools.org>) for plotting maps. Earthquakes were located using the computer code, BayesLoc (<https://gs.llnl.gov/nuclear-threat-reduction/nuclear-explosion-monitoring/bayesloc>) and relocated using hypoDD (~<https://www.ideo.columbia.edu/~felixw/hypoDD.html>). All websites were last accessed in May 2024. Finally, the supplemental material includes four figures and one table that supplement the results presented in this article.

Declaration of Competing Interests

The authors acknowledge that there are no conflicts of interest recorded.

Acknowledgments

All authors thank the captains, crew members, and scientists on board the RV Isabu and Onnuri for their cooperation and logistical support. The authors acknowledge funding from the Korea Institute of Ocean Science and Technology (KIOST) (PE99656 and PE99796), JSPS KAKENHI (Grant 18H03735), the Japan-Korea Basic Scientific Cooperation Program between JSPS and NRF (Grant Number JPJSBP120218807), and National Research Foundation of Korea (NRF) grants from the Korean government (2022R1A2C1003006 and 2022R1A5A1085103). The authors acknowledge valuable comments and suggestions from the Editor Allison Bent, Guest Editors for the focus section, and anonymous reviewers that helped improve the clarity of the article.

References

- Abercrombie, R. E., X. Chen, and J. Zhang (2020). Repeating earthquakes with remarkably repeatable ruptures on the San Andreas Fault at Parkfield, *Geophys. Res. Lett.* **47**, no. 23, e2020GL089820, doi: 10.1029/2020GL089820.
- Abrams, L. J., R. L. Larson, T. H. Shipley, and Y. Lancelot (1992). The seismic stratigraphy and sedimentary history of the East Mariana and Pigafetta basins of the western Pacific, in *Proceedings of the Ocean Drilling Program, Scientific Results*, Vol. 129, Ocean Drilling Program, College Station, Texas, 551–569.
- Allen, R. V. (1978). Automatic earthquake recognition and timing from single traces, *Bull. Seismol. Soc. Am.* **68**, no. 5, 1521–1532.
- Barchek, G., G. A. Abers, A. N. Adams, A. Bécel, J. Collins, J. B. Gaherty, P. J. Haeussler, Z. Li, G. Moore, and E. Onyango (2020). The Alaska amphibious community seismic experiment, *Seismol. Res. Lett.* **91**, no. 6, 3054–3063.
- Beavan, J., P. Tregoning, M. Bevis, T. Kato, and C. Meertens (2002). Motion and rigidity of the Pacific Plate and implications for plate boundary deformation, *J. Geophys. Res.* **107**, no. B10, ETG-19.

- Begnaud, M. L., and D. S. Stakes (2000). Constraining continental margin seismicity by extending on-shore seismograph stations to critical off-shore sites, *Bull. Seismol. Soc. Am.* **90**, no. 2, 414–424.
- Bergman, E. A. (1986). Intraplate earthquakes and the state of stress in oceanic lithosphere, *Tectonophysics* **132**, nos. 1–3, 1–35.
- Bergman, E. A., and S. C. Solomon (1980). Oceanic intraplate earthquakes: Implications for local and regional intraplate stress, *J. Geophys. Res.* **85**, no. B10, 5389–5410.
- Bergman, E. A., and S. C. Solomon (1992). On the strength of oceanic fracture zones and their influence on the intraplate stress field, *J. Geophys. Res.* **97**, no. B11, 15,365–15,377.
- Bie, L., A. Rietbrock, S. Hicks, R. Allen, J. Blundy, V. Clouard, J. Collier, J. Davidson, T. Garth, S. Goes, et al. (2020). Along-arc heterogeneity in local seismicity across the Lesser Antilles subduction zone from a dense ocean-bottom seismometer network, *Seismol. Res. Lett.* **91**, no. 1, 237–247.
- Bird, P. (2003). An updated digital model of plate boundaries, *Geochem. Geophys. Geosyst.* **4**, no. 3, 1027, doi: [10.1029/2001GC000252](https://doi.org/10.1029/2001GC000252).
- Chen, C., D. Zhao, and S. Wu (2014). Crust and upper mantle structure of the New Madrid Seismic Zone: Insight into intraplate earthquakes, *Phys. Earth Planet. Int.* **230**, nos. 1–14, doi: [10.1016/j.pepi.2014.01.016](https://doi.org/10.1016/j.pepi.2014.01.016).
- De Caro, M., C. Montuori, F. Frugoni, S. Monna, F. Cammarano, and L. Beranzoli (2020). T-phases observed at the Ionian seafloor: Seismic source and bathymetric effects, *Seismol. Res. Lett.* **92**, no. 1, 481–493.
- de Groot-Hedlin, C. D., and J. A. Orcutt (2001). Excitation of T-phases by seafloor scattering, *J. Acoust. Soc. Am.* **109**, no. 5, 1944–1954.
- Dentith, M. C., and W. E. Featherstone (2003). Controls on intraplate seismicity in southwestern Australia, *Tectonophysics* **376**, nos. 3–4, 167–184.
- Dziak, R. P. (2001). Empirical relationship of T-wave energy and fault parameters of northeast Pacific Ocean earthquakes, *Geophys. Res. Lett.* **28**, no. 13, 2537–2540.
- Dziewonski, A. M., and D. L. Anderson (1981). Preliminary reference Earth model, *Phys. Earth Planet. Int.* **25**, no. 4, 297–356.
- Eilon, Z. C., L. Zhang, J. B. Gaherty, D. W. Forsyth, and J. B. Russell (2022). Sub-lithospheric small-scale convection tomographically imaged beneath the Pacific plate, *Geophys. Res. Lett.* **49**, no. 18, e2022GL100351, doi: [10.1029/2022GL100351](https://doi.org/10.1029/2022GL100351).
- Eimer, M., D. A. Wiens, C. Cai, D. Lizarralde, and H. Jasperson (2020). Seismicity of the incoming plate and forearc near the Mariana Trench recorded by ocean bottom seismographs, *Geochem. Geophys. Geosyst.* **21**, no. 4, e2020GC008953, doi: [10.1029/2020GC008953](https://doi.org/10.1029/2020GC008953).
- Gangopadhyay, A., and P. Talwani (2003). Symptomatic features of intraplate earthquakes, *Seismol. Res. Lett.* **74**, no. 6, 863–883.
- General Bathymetric Chart of the Oceans (GEBCO) Compilation Group (2019) GEBCO 2019 Grid, doi: [10.5285/836f016a-33be-6ddc-e053-6c86abc0788e](https://doi.org/10.5285/836f016a-33be-6ddc-e053-6c86abc0788e).
- Godin, O. A. (2021). Contributions of gravity waves in the ocean to T-phase excitation by earthquakes, *J. Acoust. Soc. Am.* **150**, no. 5, 3999–4017.
- Gordon, R. G. (1998). The plate tectonic approximation: Plate non-rigidity, diffuse plate boundaries, and global plate reconstructions, *Annu. Rev. Earth Planet. Sci.* **26**, no. 1, 615–642.
- Guo, L., J. Lin, H. Yang, and J. Tian (2022). Aftershocks of the 2012 M_w 8.6 Wharton basin intraplate earthquake in the eastern Indian Ocean revealed by near-field ocean-bottom seismometers, *Seismol. Res. Lett.* **93**, no. 2A, 706–718.
- Heidbach, O., M. Rajabi, K. Reiter, M. Ziegler, and , and Wsm Team (2016). World stress map database release 2016, *GFZ Data Services*, **10**, 1, doi: [10.5880/WSM.2016.002](https://doi.org/10.5880/WSM.2016.002).
- Hirano, N., A. A. Koppers, A. Takahashi, T. Fujiwara, and M. Nakanishi (2008). Seamounts, knolls and petit-spot monogenetic volcanoes on the subducting Pacific Plate, *Basin Res.* **20**, no. 4, 543–553.
- Kaneda, K., S. Kodaira, A. Nishizawa, T. Morishita, and N. Takahashi (2010). Structural evolution of preexisting oceanic crust through intraplate igneous activities in the Marcus-Wake seamount chain, *Geochem. Geophys. Geosyst.* **11**, no. 10, doi: [10.1029/2010GC003231](https://doi.org/10.1029/2010GC003231).
- Kawakatsu, H., and H. Utada (2017). Seismic and electrical signatures of the lithosphere–asthenosphere system of the normal oceanic mantle, *Annu. Rev. Earth Planet. Sci.* **45**, 139–167.
- Kawano, Y., T. Isse, H. Kawakatsu, H. Shiobara, N. Takeuchi, H. Sugioka, Y. Kim, H. Utada, and S. M. Lee (2023). Noise reduction from vertical-component seismograms recorded by broadband ocean-bottom seismometers deployed at the western Pacific, *Bull. Seismol. Soc. Am.* **113**, no. 4, 1759–1771.
- Kim, T. S., J. H. Park, J. W. Ko, S. Y. Oh, M. Witek, S. J. Chang, S. M. Lee, Y. H. Kim, H. Utada, and H. Kawakatsu (2023). Characteristics of background noise in the Oldest-1 array deployed on the Oldest part of the Pacific Plate, *Bull. Seismol. Soc. Am.* **113**, no. 4, 1772–1793.
- Kim, W. Y. (2013). Induced seismicity associated with fluid injection into a deep well in Youngstown, Ohio, *J. Geophys. Res.* **118**, no. 7, 3506–3518.
- Kim, W. Y., L. Ottemöller, and P. G. Richards (2020). A regional Sn magnitude scale mb (Sn) and estimates of moment magnitude for earthquakes along the Northern Mid-Atlantic Ridge, *Bull. Seismol. Soc. Am.* **110**, no. 6, 3158–3173.
- Klein, F. W. (2016). Lithospheric flexure under the Hawaiian volcanic load: Internal stresses and a broken plate revealed by earthquakes, *J. Geophys. Res.* **121**, no. 4, 2400–2428.
- Kreemer, C., G. Blewitt, and E. C. Klein (2014). A geodetic plate motion and Global Strain Rate Model, *Geochem. Geophys. Geosyst.* **15**, no. 10, 3849–3889.
- Levy, S., D. R. Bohnenstiehl, P. Sprinkle, M. S. Boettcher, W. S. D. Wilcock, M. Tolstoy, and F. Waldhauser (2018). Mechanics of fault reactivation before, during, and after the 2015 eruption of Axial Seamount, *Geology* **46**, no. 5, 447–450.
- Lowrie, A., C. Smoot, and R. Batiza (1986). Are oceanic fracture zones locked and strong or weak?: New evidence for volcanic activity and weakness, *Geology* **14**, no. 3, 242–245.
- Maggi, A., E. Debayle, K. Priestley, and G. Barruol (2006). Multimode surface waveform tomography of the Pacific Ocean: a closer look at the lithospheric cooling signature, *Geophys. J. Int.* **166**, no. 3, 1384–1397.
- McGovern, P. J. (2007). Flexural stresses beneath Hawaii: Implications for the October 15, 2006, earthquakes and magma ascent, *Geophys. Res. Lett.* **34**, no. 23, doi: [10.1029/2007GL031305](https://doi.org/10.1029/2007GL031305).
- McNamara, D. E., and R. P. Buland (2004). Ambient noise levels in the continental United States, *Bull. Seismol. Soc. Am.* **94**, no. 4, 1517–1527.

- Morrow, T. A., E. Mittelstaedt, and S. S. Kim (2019). Are segmented fracture zones weak? Analytical and numerical models constrain anomalous bathymetry at the Clarion and Murray fracture zones, *Earth Planet. Sci. Lett.* **512**, 214–226.
- Müller, R. D., S. Zahirovic, S. E. Williams, J. Cannon, M. Seton, D. J. Bower, M. G. Tetley, C. Heine, E. L. Breton, and S. Liu (2019). A global plate model including lithospheric deformation along major rifts and orogens since the Triassic, *Tectonics* **38**, no. 6, 1884–1907.
- Myers, S. C., G. Johannesson, and W. Hanley (2007). A Bayesian hierarchical method for multiple-event seismic location, *Geophys. J. Int.* **171**, no. 3, 1049–1063.
- Myers, S. C., G. Johannesson, and W. Hanley (2009). Incorporation of probabilistic seismic phase labels into a Bayesian multiple-event seismic locator, *Geophys. J. Int.* **177**, no. 1, 193–204.
- Nakanishi, M., K. Tamaki, and K. Kobayashi (1992). Magnetic anomaly lineations from Late Jurassic to Early Cretaceous in the west-central Pacific Ocean, *Geophys. J. Int.* **109**, no. 3, 701–719.
- Okal, E. (1984). Intraplate seismicity of the southern part of the Pacific plate, *J. Geophys. Res.* **89**, no. B12, 10,053–10,071.
- Ross, Z. E., D. T. Trugman, E. Hauksson, and P. M. Shearer (2019). Searching for hidden earthquakes in Southern California, *Science* **364**, no. 6442, 767–771.
- Sandwell, D. T. (1984). Thermomechanical evolution of oceanic fracture zones, *J. Geophys. Res.* **89**, no. B13, 11,401–11,413.
- Schaff, D. P., and F. Waldhauser (2005). Waveform cross-correlation-based differential travel-time measurements at the Northern California Seismic Network, *Bull. Seismol. Soc. Am.* **95**, no. 6, 2446–2461.
- Schulte, S. M., and W. D. Mooney (2005). An updated global earthquake catalogue for stable continental regions: Reassessing the correlation with ancient rifts, *Geophys. J. Int.* **161**, no. 3, 707–721.
- Shen, Y. (2002). Seismicity at the southern East Pacific Rise from recordings of an ocean bottom seismometer array, *J. Geophys. Res.* **107**, no. B12, EPM-9.
- Shinohara, M., T. Fukano, T. Kanazawa, E. Araki, K. Suyehiro, M. Mochizuki, K. Nakahigashi, T. Yamada, and K. Mochizuki (2008). Upper mantle and crustal seismic structure beneath the Northwestern Pacific Basin using a seafloor borehole broadband seismometer and ocean bottom seismometers, *Phys. Earth Planet. Int.* **170**, nos. 1–2, 95–106.
- Shiobara, H., A. Ito, H. Sugioka, M. Shinohara, and T. Sato (2021). Tilt observations at the seafloor by mobile ocean bottom seismometers, *Front. Earth Sci.* **8**, 599810, doi: [10.3389/feart.2020.599810](https://doi.org/10.3389/feart.2020.599810).
- Stähler, S. C., K. Sigloch, K. Hosseini, W. C. Crawford, G. Barruol, M. C. Schmidt-Aursch, M. Tsekhnistrenko, J. R. Scholz, A. Mazullo, and M. Deen (2016). Performance report of the RHUM-RUM ocean bottom seismometer network around La Réunion, western Indian Ocean, *Adv. Geosci.* **41**, 43–63.
- Suetsugu, D., and H. Shiobara (2014). Broadband ocean-bottom seismology, *Annu. Rev. Earth Planet. Sci.* **42**, no. 1, 27–43.
- Sumy, D. F., J. A. Lodewyk, R. L. Woodward, and B. Evers (2015). Ocean-bottom seismograph performance during the Cascadia initiative, *Seismol. Res. Lett.* **86**, no. 5, 1238–1246.
- Tan, Y., and D. V. Helmberger (2007). Trans-Pacific upper mantle shear velocity structure, *J. Geophys. Res.* **112**, no. B8, doi: [10.1029/2006JB004853](https://doi.org/10.1029/2006JB004853).
- Tréhu, A. M., J. Braunmiller, and E. Davis (2015). Seismicity of the central Cascadia continental margin near 44.5 N: A decadal view, *Seismol. Res. Lett.* **86**, no. 3, 819–829.
- Tréhu, A. M., W. S. Wilcock, R. Hilmo, P. Bodin, J. Connolly, E. C. Roland, and J. Braunmiller (2018). The role of the Ocean Observatories Initiative in monitoring the offshore earthquake activity of the Cascadia subduction zone, *Oceanography* **31**, no. 1, 104–113.
- Trnkoczy, A. (2009). Understanding and parameter setting of STA/LTA trigger algorithm, *New manual of seismological observatory practice* 1–20.
- Uchida, N., and R. Bürgmann (2019). Repeating earthquakes, *Annu. Rev. Earth Planet. Sci.* **47**, 305–332.
- Waldhauser, F. (2001). hypoDD—A program to compute double-difference hypocenter locations, *Open-File Rept. 2001-113* doi: [10.3133/ofr01113](https://doi.org/10.3133/ofr01113).
- Waldhauser, F., and W. L. Ellsworth (2000). A double-difference earthquake location algorithm: Method and application to the northern Hayward fault, California, *Bull. Seismol. Soc. Am.* **90**, no. 6, 1353–1368.
- Waldhauser, F., and D. P. Schaff (2021). A comprehensive search for repeating earthquakes in northern California: Implications for fault creep, slip rates, slip partitioning, and transient stress, *J. Geophys. Res.* **126**, no. 11, e2021JB022495, doi: [10.1029/2021JB022495](https://doi.org/10.1029/2021JB022495).
- Walker, D. A., and C. S. McCreery (1985). Significant unreported earthquakes in “aseismic” regions of the Western Pacific, *Geophys. Res. Lett.* **12**, no. 7, 433–436.
- Walker, D. A., C. S. McCreery, and Y. Hiyoshi (1992). T-phase spectra, seismic moments, and tsunamigenesis, *Bull. Seismol. Soc. Am.* **82**, no. 3, 1275–1305.
- Webb, S. C. (1998). Broadband seismology and noise under the ocean, *Rev. Geophys.* **36**, no. 1, 105–142.
- Wessel, P., and W. F. Haxby (1990). Thermal stresses, differential subsidence, and flexure at oceanic fracture zones, *J. Geophys. Res.* **95**, no. B1, 375–391.
- Wiens, D. A., and S. Stein (1983). Age dependence of oceanic intraplate seismicity and implications for lithospheric evolution, *J. Geophys. Res.* **88**, no. B8, 6455–6468.
- Wiens, D. A., and S. Stein (1985). Implications of oceanic intraplate seismicity for plate stresses, driving forces and rheology, *Tectonophysics* **116**, nos. 1–2, 143–162.
- Williams, C. M., R. A. Stephen, and D. K. Smith (2006). Hydroacoustic events located at the intersection of the Atlantis (30° N) and Kane (23° 40' N) Transform Faults with the Mid-Atlantic Ridge, *Geochem. Geophys. Geosyst.* **7**, no. 6, doi: [10.1029/2005GC001127](https://doi.org/10.1029/2005GC001127).
- Withers, M., R. Aster, C. Young, J. Beiriger, M. Harris, S. Moore, and J. Trujillo (1998). A comparison of select trigger algorithms for automated global seismic phase and event detection, *Bull. Seismol. Soc. Am.* **88**, no. 1, 95–106.
- Wysession, M. E., E. A. Okal, and K. L. Miller (1991). Intraplate seismicity of the Pacific Basin, 1913–1988, *Pure Appl. Geophys.* **135**, 261–359.

Manuscript received 26 August 2024
Published online 13 December 2024